Large-Scale Synthesis of Transition-metal Doped TiO_2 Nanowires with Controllable Overpotential

Bin Liu[1]‡, Hao Ming Chen,[1]‡ Chong Liu[1,3], Sean C. Andrews[1,3], Chris Hahn[1], Peidong Yang[1,2,3,*]

[1]Department of Chemistry, University of California, Berkeley, California 94720, USA

[2]Department of Materials Science and Engineering, University of California, Berkeley, California 94720, USA

[3]Materials Sciences Division, Lawrence Berkeley National Laboratory, Berkeley, California 94720, USA

Supporting Information Placeholder

ABSTRACT: Practical implementation of one-dimensional semiconductors into devices capable of exploiting their novel properties is often hindered by low product yields, poor material quality, high production cost, or overall lack of synthetic control. Here, we show that a molten-salt flux scheme can be used to synthesize large quantities of high quality, single crystalline TiO2 nanowires with controllable dimensions. Furthermore, in situ dopant incorporation of various transition metals allows for the tuning of optical, electrical, and catalytic properties. With this combination of control, robustness, and scalability, the molten-salt flux scheme can provide high quality TiO2 nanowires to satisfy a broad range of application needs ranging from photovoltaics to photocatalysis.

Over the past two decades, tremendous effort has been directed towards the synthesis of one-dimensional materials, whose unique chemical/physical properties can potentially be exploited in various fields, including optoelectronic, photovoltaic, electrochemical, and electromechanical devices.[1-9] Many synthetic methods have been developed for growing one-dimensional (1D) semiconductors, including vapor-liquid-solid (VLS),[10,11] vapor-solid (VS),[12] solution-liquid-solid (SLS),[13] and hydrothermal/solvothermal techniques.[14-16] However, these methods typically trade either yield for quality or vice versa. Since the future of 1D semiconductor nanotechnology depends on the balance between materials yield and subsequent device performance,[17] development of synthetic routes capable of simultaneously satisfying the needs of high yield, large-scale production, and high material quality continues to require great ingenuity. Molten salt flux synthesis is accomplished by utilizing a mixture of molten salts as a highly reactive medium, where there is facile diffusion in the liquid state. Eutectic salt compositions are commonly utilized for maximal reactivity at their respective minimal required temperature, where the mobility of ions in these molten salts is approximately 10^{10} times higher than in the solid state.[18] Once the product material is less soluble than the reactants in the salt solution, various salt mixtures can be tailored to the reactants and subsequent products of choice.[19,20]

Herein, we report a molten salt synthetic route to synthesize large quantities of high quality, single crystalline TiO_2 nanowires. In this technique, commercially available TiO_2 nanoparticles and common salt mixtures are chosen as the raw material and reaction medium, respectively. This molten-salt flux scheme significantly improves the nanowire yield while maintaining high crystal quality and illustrates the feasibility of large scale production of semiconductor nanowires. We additionally demonstrate that this method allows for incorporation of various transition-metal (TM) dopants into the TiO_2 lattice by introducing the corresponding TM salt as a dopant source. The homogeneity of the dopant speciation exhibits simultaneous benefits in both the optical properties and photocatalytic response of the TiO_2 nanowires.

In a typical synthesis, the present molten-salt flux method involves a blended mixture of TiO_2 nanoparticles, NaCl, and Na_2HPO_4, which is heated above the melting point of the salt mixture to achieve a large-scale synthesis of TiO_2 nanowires with a yield of about 99% (Figure 1a). X-ray diffraction (XRD) collected under synchrotron radiation light source (λ = 0.7749 Å) shows the absence of any peaks other than the tetragonal rutile phase of TiO_2 (Figure 1b). Scanning electron microscopy (SEM) confirmed the 1D nanowire morphology and revealed both uniform diameters of 100 nm and variable length from 5 to 40 μm, resulting in exceptionally large aspect ratios of up to 400 (Figure 1c and d). A representative transmission electron microscopy (TEM) image and diffraction pattern seen in Figure 1e confirms the nanowires are grown along the [001] direction and bounded by four {100} facets on the side wall, as evidenced by the sharp selected area electron diffraction patterns examined along and [100] zone axis. The end tips, however, consist of four {011} facets focused to a point, where the tip angle matches nearly exactly to the theoretical value of 113.88° (along the [100] zone axis). Examination of individual nanowires with HRTEM shows that they are completely crystalline along their entire lengths (Figure 1f). Lattice fringes with interplanar spacings d_{100} = 4.5 ± 0.2 Å and d_{001} = 2.9 ± 0.1 Å are measured and are consistent with the rutile crystal structure. To investigate the nanowire formation mechanism, aliquoted products were examined ex-situ. When heated above 600 °C for more than 2 minutes, the percentage of anatase diffraction in the reaction product was reduced compared to the unheated mixture of P25 nanoparticles, NaCl and Na_2HPO_4 (Figure S1 and S2)(Supporting Information). Concurrently, a new phase of monoclinic tetrasodium titanium nonaoxodiphosphate ($Na_4TiP_2O_9$) was observed.[21] After 8 minutes of heating at 825 °C, the formation of the $Na_4TiP_2O_9$ intermediate plays a critical role for rutile nanowire growth, as evidenced by the necessity of its formation to produce TiO_2 nanowires. Attempts using only NaCl or Na_2HPO_4 resulted in only rutile TiO_2 particles (Figure S3). A mixture of NaCl (80 wt%) and Na_2HPO_4 (20 wt%) achieves the lowest eutectic temperature and is shown to be the eutectic composition with the present reac-

tion temperature (825 °C) according to the phase diagram,[19] meaning that the molten environment maximizes the solubility and diffusivity of the reactant.

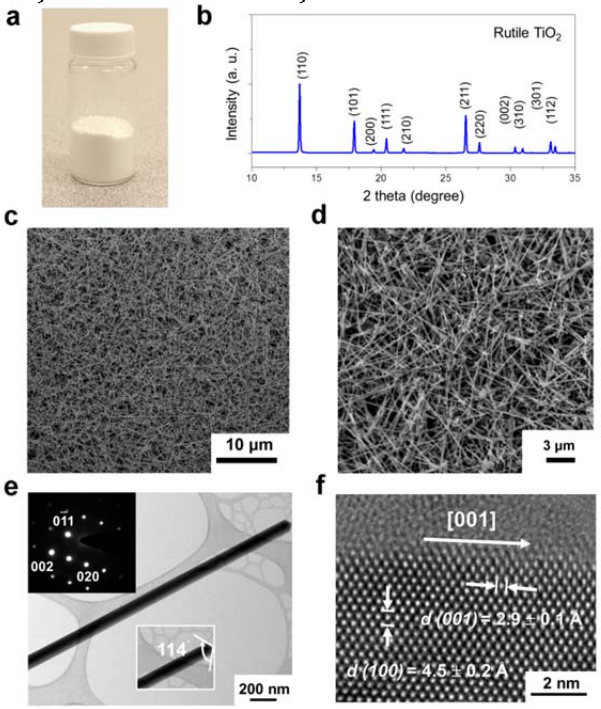

Figure 1. (a) photograph of rutile TiO_2 nanowires. (b) XRD pattern of as-prepared TiO_2 nanowires. (c) and (d) SEM image of rutile TiO_2 nanowires. (e) TEM image of a single TiO_2 nanowire examined along the [100] zone axis. Insets show the corresponding SAED pattern and tip angle. (f) HRTEM image of a single TiO_2 nanowire.

In addition to the influence of the salt mixture, variations of the reactant phase yielded controllable differences in the products. Anatase, the metastable phase of TiO_2, readily reacts with $Na_4P_2O_7$ to form $Na_4TiP_2O_9$ at temperatures above 600 °C,[22] while the thermodynamically stable rutile phase does not form this intermediate under present condition. Consequently, pure anatase particles could be used as titanium source to synthesis rutile nanowires as well (Figure S4); however, rutile nanowires synthesized from pure anatase particles have broader size distributions, suggesting that the synthesis of rutile nanowires is optimally performed through P25 nanoparticles containing both anatase and rutile phases, wherein they serve dual roles as both rutile seeds and TiO_2 nutrients. Anisotropic crystal growth of nanowires along the rutile *c*-axis results from lower solid-liquid interfacial energy and free energy minimization for growth occurring parallel to the [001] direction.[23] The (011) facets observed at the tips of the nanowires work in concert with the (100) facet along the nanowire length to minimize the total surface energy, resulting in the formation of rutile nanowires with rectangular cross sections.[24]

In addition to large yield of the single crystalline nanowires, this synthetic scheme also allows for the introduction of transition-metal dopants. Historically, a variety of these transition-metals have been explored as dopants in modifying the electronic structure of TiO_2 to improve its visible-light photocatalytic activity.[25-28] Because of the interaction between t_{2g} state of TM-dopants and Ti atoms, transition-metal doping could considerably create an additionally occupied state in the bandgap of TiO_2.[25] Here, through the introduction of transition-metal dopants such as V, Cr, Mn, Fe, Co, Nb, Mo, and Rh, during the molten salt synthesis, the as-prepared 2% TM-doped of TiO_2 nanowires (Figure S5) exhibit a variety of colors, departing from the white color of the undoped product. For instance, Rh-doped samples show a deep brown color resulted from the strong absorption in visible region (Figure 2). Consequently, the light absorption edge of transition-metal doped TiO_2 nanowires extends from ultraviolet to visible, increasing the overlap between light absorption and the solar spectrum, thereby widening the range of sunlight that is able to be captured to generate photoelectrons for photocatalytic reactions.

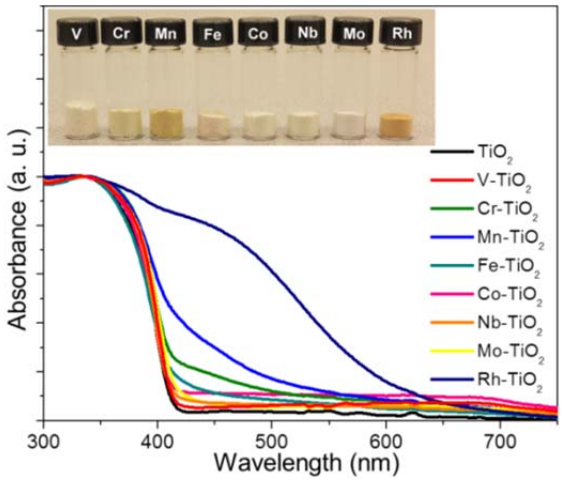

Figure 2. Photograph of various transition-metal doped TiO_2 nanowires and UV-vis spectra of various transition-metal doped TiO_2 nanowires.

Since the photocatalytic properties of transition-metal doping of TiO_2 nanowires can be strongly affected by the dopant speciation and position, X-ray diffraction via synchrotron radiation was used to confirm that only the tetragonal rutile phase of TiO_2 exists in the doped samples (Figure 3a). This indicates that the optical variation can be attributed to the metal doping rather than the formation of undesired phases that may have been created as a result of adding dopant precursors to the reaction mixture. In order to probe short-range structure, extended X-ray absorption fine structure (EXAFS) spectra were collected for specific nearest-neighbor interatomic distances and coordination numbers.[29] Rutile has a tetragonal crystal structure, in which each Ti atom is surrounded by six O atoms in octahedral coordination, with two distinct bond lengths of 1.947 Å and 1.981 Å (Figure 3b). Correspondingly, three major peaks were present in the Fourier-transforms (FT) of the EXAFS data (Figure 3c). The first peak at ~1.8 Å of the FT EXAFS signal (first shell) obtained after phase correction is due to both families of O atoms. The second peak at ~2.7 Å of the FT is assigned to single scattering by Ti-Ti atoms occupying the centers of contiguous rectangular prisms (2nd), while the third peak at ~3.4 Å is in part due to the eight Ti atoms occupying the vertices of the prism and in part to multiple scattering contributions from both Ti and O atoms (3rd). The second shell exhibits a significant change in both position or shape in various transition-metal doping, revealing that the transition metal atoms substitute for Ti atoms at the same site around Ti atoms. Since the first shell was due to the single scattering

of O atoms and several multiple scattering were involved in the third shell, these two shells give no additional information about the dopant position. Therefore, only the second shell was refined to extract quantitative structural parameters (Table 1). The Ti-Ti contribution at a distance of 3.01 Å for rutile TiO_2 nanowires and the coordination number around 1.93 is consistent with the bulk value of rutile TiO_2 (JCPDS file no. 88-1175). With regard to the transition-metal doping, considerable contribution from the single scattering of transition-metals around Ti atoms were present in various cases of doped TiO_2 samples, revealing the transition-metal atoms significantly exist around absorbing Ti atoms. Although the coordination number (CN) for Ti-TM (transition-metal) path cannot precisely reflect the doping amount in rutile crystal due to low concentration of dopants (2%), this result still demonstrates the effectiveness of doping with TM in present molten salt method. HRTEM images of TM-doped TiO_2 nanowires further demonstrate that neither crystal defects nor other phases can be observed (Figure 3d). Furthermore, this synthetic route enables doping to occur before the subsurface layer begins to suffer from phase transformation and degradation, as is a common problem from diffusion-based, post-growth methods. In situ dopant incorporation allows for homogeneous dopant distributions, which can exhibit higher charge carrier mobility and higher visible-light absorbance than that of surface doping.[25]

To examine the transport and photoelectrochemical properties, nanowire electrodes were fabricated by drop-casting nanowires onto FTO substrates. From the slopes of the Mott-Schottky plots (Figure 4a & S6), carrier densities of undoped and 2 % Nb doped TiO_2 nanowires were estimated to be ~10^{15} and ~10^{21} cm^{-3}, respectively, using the following relation: $N_d = (2/e_0\varepsilon\varepsilon_0)[d(1/C^2)/dV]^{-1}$, where e_0 is the electron charge, ε is the rutile TiO_2 dielectric constant (ε = 86),[30] ε_0 is the vacuum permittivity, and N_d is the donor density.[31] The positive slope indicates n-type behavior of the rutile nanowires. The low carrier density of the undoped sample reflects the high crystalline quality of the rutile nanowires, which is a result of the high temperature used in the molten salt synthesis.

Dopant incorporation not only allows for flexibility to tune the carrier concentration of TiO_2, but also beneficially affects its photocatalytic performance. It is well-known that TiO_2 can be used as a photocatalyst for the photoelectrolysis of water.[32] However, the large overpotential for the oxygen evolution reaction (OER) to occur commonly limits its performance. However, the introduction of transition-metal dopants uniformly into TiO_2 lattice exhibits substantial decreases to the overpotential (Figure 4b), where the overpotential are compared in a specific current density of 0.5 mA/cm^2. Since the OER overpotential is affected by the binding energy with intermediates such as O^*, HO^* and HOO^*, transition metal dopants can lead lower overpotentials due to stronger interactions of the adsorbed species on the surface.[33] We obtained a minimum overpotential of 0.488 V on 2% Mn-doped TiO_2 nanowires, this represents a ~28% decrease in overpotential relative to pristine rutile TiO_2 (Table 2), which indicated that transition-metal substitutions on TiO_2 crystal are able to alter the adsorption energy of reaction intermediates for OER in spite of low quantity of dopant. Several theoretical predictions of overpotentials are listed in Table 2 for comparison, in which 6.25% Mn-doped on rutile TiO_2 single crystal exhibited a decrease in overpotential by 48%. While this prediction is greater than the measured reduction, this discrepancy might be due to a lower substitution ratio than what was performed in theoretical simulation. Although the determination of overpotential was experimentally current-dependence, the absolute values from predication and experiment cannot be directly compared, but the trends can be compared relatively. Our observed OER overpotential of various transition-metal doping occurs in the sequence Mn-TiO_2<Mo-TiO_2<Nb-TiO_2<TiO_2, which follows the same trend as theoretic simulation even with the difference in dopant concentration.[32]

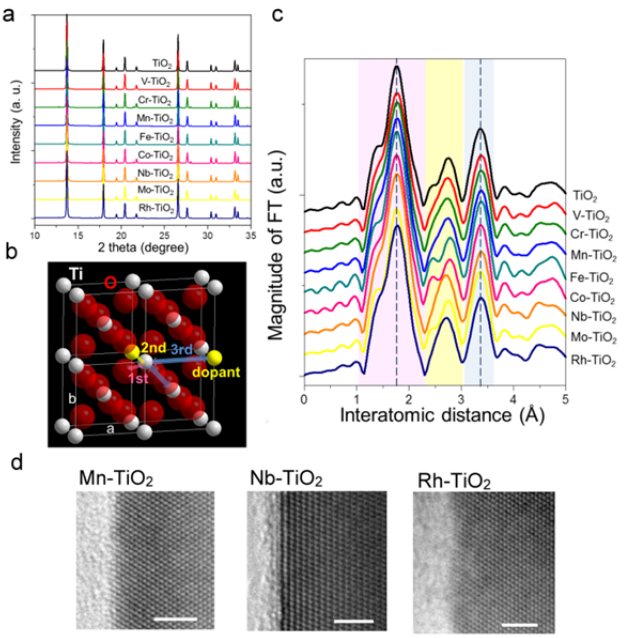

Figure 3. (a) XRD patterns of transition-metal doped TiO_2 nanowires, showing that there were no impurities forming in various dopants samples. (b) Rutile structure of TiO_2 and scattering shell modes around Ti atom. (c) FT EXAFS spectra of various transition-metal doped samples, (d) HRTEM images of the rutile TiO_2 nanowires with doping of Mn, Nb, and Rh (scale bar, 2 nm).

In summary, the successful utilization of the molten-salt flux method allows for the synthesis of TiO_2 nanomaterials in large quantities, which has the potential for mass production in future nanomaterial production. Transition-metal doping allows for tunable optical absorption for tailored capture of visible light, as well as decreases of the OER overpotential in the electrolysis of water. TiO2 is commonly employed as a photocatalyst rather electrocatalyst owing to its intrinsically low carrier concentration and poor conductivity. However, both improving its conductivity and decreasing OER overpotential through transition-metal doping are able to be expected to benefit its photoactivity especially for water oxidation and considerably suppress this kinetic loss of overpotential. Considering the advantage and versatility offered by this molten salt method, the findings here can have an important impact in making large scale, tunable, and durable synthesis of various one dimensional materials a reality.

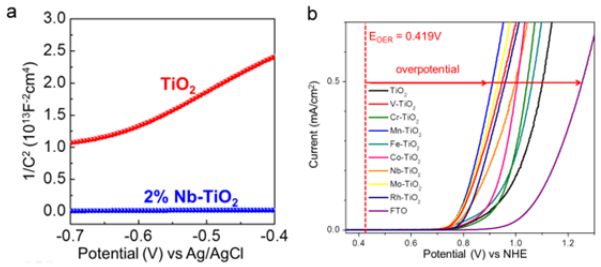

Figure 4. (a) Mott-Schottky plot of a TiO_2 and 2% Nb-TiO_2 nanowire electrode measured at 500 Hz. (b) Overpotential measurement for oxygen evolution reaction using FTO, TiO_2 nanowire with/without transition-metal doping electrodes in basic solutions. Dashed vertical lines represent the thermodynamic redox potential for water oxidation at the pH~13.6.

Table 1.Experimental overpotential associated with OER on TM-doped TiO_2 nanowires and theoretical calculation from TM-doped rutile TiO_2 single crystal

Sample (2% dopants)	Overpotential (at 0.5 mA/cm^2)	Calculated overpotential (6.25% dopants)[32]
FTO	0.836 V	--
TiO_2	0.681 V	1.3 V
V-TiO_2	0.529 V	--
Cr-TiO_2	0.623 V	--
Mn-TiO_2	0.488 V	0.69 V
Fe-TiO_2	0.644 V	--
Co-TiO_2	0.586 V	--
Nb-TiO_2	0.578 V	0.76 V
Mo-TiO_2	0.514 V	0.74 V
Rh-TiO_2	0.539 V	--

ASSOCIATED CONTENT

Supporting Information

Experimental details, Figure S1-S6, and Table S1. This material is available free of charge via the Internet at http://pubs.acs.org.

AUTHOR INFORMATION

Corresponding Author

p_yang@berkeley.edu

Author Contributions

‡These authors contributed equally.

Notes

The authors declare no competing financial interests.

ACKNOWLEDGMENT

This work was supported by the Director, Office of Science, Office of Basic Energy Sciences, Materials Sciences and Engineering Division, of the U. S. Department of Energy under Contract No. DE-AC02-05CH11231.

REFERENCES

(1) Xia, Y. N.; Yang, P. D.; Sun, Y. G.; Wu, Y. Y.; Mayers, B.; Gates, B.; Yin, Y. D.; Kim, F.; Yan, Y. Q. *Adv. Mater.* **2003**, *15*, 353.
(2) Law, M.; Goldberger, J.; Yang, P. D. *Annu. Rev. of Mater. Res.* **2004**, *34*, 83.
(3) Hochbaum, A. I.; Yang, P. D. *Chem. Rev.* **2010**, *110*, 527.
(4) Huang, M. H.; Mao, S.; Feick, H.; Yan, H. Q.; Wu, Y. Y.; Kind, H.; Weber, E.; Russo, R.; Yang, P. D. *Science* **2001**, *292*, 1897.
(5) Law, M.; Greene, L. E.; Johnson, J. C.; Saykally, R.; Yang, P. D. *Nat. Mater.* **2005**, *4*, 455.
(6) Law, M.; Sirbuly, D. J.; Johnson, J. C.; Goldberger, J.; Saykally, R. J.; Yang, P. D. *Science* **2004**, *305*, 1269.
(7) Tang, J. Y.; Huo, Z. Y.; Brittman, S.; Gao, H. W.; Yang, P. D. *Nat. Nanotechnol.* **2011**, *6*, 568.
(8) Cui, Y.; Wei, Q. Q.; Park, H. K.; Lieber, C. M. *Science* **2001**, *293*, 1289.
(9) Chan, C. K.; Peng, H. L.; Liu, G.; McIlwrath, K.; Zhang, X. F.; Huggins, R. A.; Cui, Y. *Nat. Nanotechnol.* **2008**, *3*, 31.
(10) Morales, A. M.; Lieber, C. M. *Science* **1998**, *279*, 208.
(11) Wu, Y. Y.; Yang, P. D. *J. Am. Chem. Soc.* **2001**, *123*, 3165.
(12) Yang, P. D.; Lieber, C. M. *Science* **1996**, *273*, 1836.
(13) Trentler, T. J.; Hickman, K. M.; Goel, S. C.; Viano, A. M.; Gibbons, P. C.; Buhro, W. E. *Science* **1995**, *270*, 1791.
(14) Liu, B.; Aydil, E. S. *J. Am. Chem. Soc.* **2009**, *131*, 3985.
(15)Morin, S. A.; Bierman, M. J.; Tong, J.; Jin, S. *Science* **2010**, *328*, 476.
(16) Greene, L. E.; Law, M.; Goldberger, J.; Kim, F.; Johnson, J. C.; Zhang, Y. F.; Saykally, R. J.; Yang, P. D. *Angew. Chem. Int. Ed.* **2003**, *42*, 3031.
(17) Yang, P. D.; Yan, R. X.; Fardy, M. *Nano Lett.* **2010**, *10*, 1529.
(18) Arendt, R. H.; Rosolowski, J. H.; Szymaszek, J. W. *Mater. Res. Bull.* **1979**, *14*, 703.
(19) Roy, B.; Ahrenkiel, S. P.; Fuierer, P. A. *J. Am. Ceram. Soc.* **2008**, *91*, 2455.
(20) Roy, B.; Fuierer, P. A. *J. Am. Ceram. Soc.* **2010**, *93*, 436.
(21) Bolotina, N. B.; Maximov, B. A.; Petricek, V.; Simonov, V. I. *Kristallografiya* **1995**, *40*, 611.
(22) Kabbour, H.; Coillot, D.; Colmont, M.; Masquelier, C.; Mentre, O. *J. Am. Chem. Soc.* **2011**, *133*, 11900.
(23) Oliver, P. M.; Watson, G. W.; Kelsey, E. T.; Parker, S. C. *J. Mater. Chem.* **1997**, *7*, 563.
(24) Ramamoorthy, M.; Vanderbilt, D.; Kingsmith, R. D. *Phys. Rev. B* **1994**, *49*, 16721.
(25) Liu, G.; Wang, L.; Yang, H. G.; Cheng, H.-M.; Lu, G. Q. *J. Mater. Chem.* **2010**, *20*, 831.
(26) Bak, T.; Nowotny, J.; Rekas, M.; Sorrell, C. C. *Int. J. Hydrogen Energ.* **2002**, *27*, 991.
(27) Janisch, R.; Gopal P.; Spaldin N. A. *J. Phys.: Condens. Matter* **2005**, *17*, R657.
(28) Wang, Y.; Hao, Y.; Cheng, H.; Ma, J.; Xu, B.; Li, W.; Cai, S. *J. Mater. Sci.* **1999**, *34*, 2773.
(29) Iwasawa, Y. X-ray Absorption Fine Structure for Catalysts and Surfaces; World Scientific: Singapore, 1996.
(30) Parker, R. A. *Physical Review* **1961**, *124*, 1719.
(31) Furubayashi, Y.; Hitosugi, T.; Yamamoto, Y.; Inaba, K.; Kinoda, G.; Hirose, Y.; Shimada, T.; Hasegawa, T. *Appl. Phys. Lett.* **2005**, 86, 252101.
(32) Fujishima, A.; Honda, K. *Nature* **1972**, *238*, 37.
(33) Garcia-Mota, M.; Vojvodic, A.; Metiu, H.; Man, I. C.; Su, H. Y.; Rossmeisl, J.; Norskov, J. K. *Chemcatchem* **2011**, *3*, 1607.

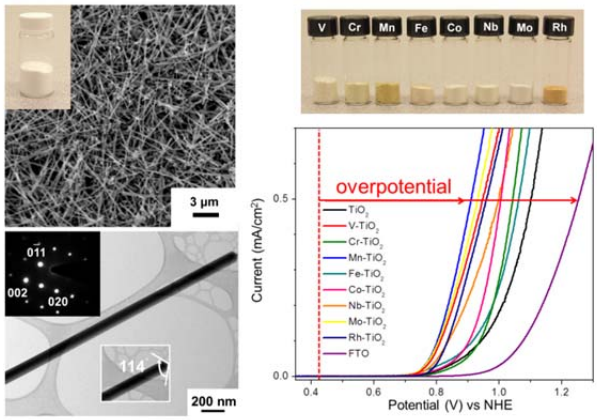
3 μm
011
002
020
114
200 nm
V
Cr
Mn
Fe
Co
Nb
Mo
Rh
overpotential
Current (mA/cm²)
0.5
0.0
0.4
0.6
0.8
1.0
1.2
Potential (V) vs NHE
TiO2
V-TiO2
Cr-TiO2
Mn-TiO2
Fe-TiO2
Co-TiO2
Nb-TiO2
Mo-TiO2
Rh-TiO2
FTO

Acknowledgements: This work was supported by the Director, Office of Science, Office of Basic Energy Sciences, Material Sciences and Engineering Division, of the U.S. Department of Energy under Contract No. DE-AC02-05CH11231. We thank the National Center for Electron Microscopy for the use of their facilities.